

Different roles of dynamic and thermodynamic effects in enhanced semi-arid warming

Ruixia Guo,¹ Xiaodan Guan,^{1*} Yongli He, Zewen Gan and Hongchun Jin

Key Laboratory for Semi-arid Climate Change of the Ministry of Education, College of Atmospheric Sciences, Lanzhou University, China

ABSTRACT: Enhanced warming in semi-arid regions has received much attention since it was first proposed, but the primary driver of this phenomenon remains unknown. This study applied dynamical adjustment to surface air temperature and partitioned the warming into two separate components: a thermodynamically forced component and a dynamically induced component. The results show that the mean amount of thermodynamic warming in the Northern Hemisphere in the study period 1902–2011 was 1.36 °C/109 years and that the amount of dynamic warming was 0.14 °C/109 years. In the mid-latitude zones of Asia, Europe, and North America, the thermodynamic warming was 1.60, 1.19, and 1.32 °C/109 years, respectively, and the corresponding dynamic warming was 0.26, 0.14, and 0.09 °C/109 years. Obviously, higher thermodynamic temperature warming was observed in semi-arid regions, suggesting that the enhanced semi-arid warming (ESAW) is the result of local thermodynamic effects. Thus, different local thermodynamic effects are responsible for the warming discrepancies in the semi-arid regions of Asia, Europe, and North America. Moreover, the considerable bias of Coupled Model Intercomparison Project Phase 5 (CMIP5) ensemble mean temperature trend appeared in semi-arid regions rather than other regions indicate that the simulation of semi-arid regions is particularly complex and difficult.

KEY WORDS thermodynamic warming; dynamic warming; semi-arid regions

Received 29 August 2016; Revised 28 March 2017; Accepted 27 April 2017

1. Introduction

Since 1970s, increasing scientific evidence has shown that global warming is occurring. Indeed, multiple independent climate indicators, including changes in land cover, atmospheric and oceanic temperatures, glaciers, snow cover, sea ice, sea level, and atmospheric water vapour, have demonstrated that the air temperature is increasing (IPCC, 2013). However, the temperature change has not been uniform, instead exhibiting marked seasonal and regional variations. The temperature over land has increased more rapidly than that over ocean, and the land/sea warming ratio has varied in the range of 1.36–1.84 (Sutton *et al.*, 2007). Additionally, different warming trends were found in the cold and warm seasons over different climatic regions. Previous studies have reported that the semi-arid areas over the mid-to-high latitudes in the Northern Hemisphere (NH) have experienced particularly enhanced warming during the boreal cold seasons (Huang *et al.*, 2012). Using the ensemble empirical mode decomposition method, Ji *et al.* (2014) investigated the accumulated warming in cold seasons from 1901 to 2009. They found that the semi-arid regions of NH mid-latitude experienced the strongest warming in the last century.

Enhanced semi-arid warming (ESAW) is an obvious signal in the mid-to-high latitudes of the NH and the study of this warming is crucial for understanding the non-uniformity of global warming. ESAW is the result of various factors, including continental and local effects (Huang *et al.*, 2012). The dynamically induced component of this warming is thought to be dominated by internal variability in the climate system represented by the Atlantic multi-decadal oscillation (AMO) (Chylek *et al.*, 2014; Mann *et al.*, 2014), the north Atlantic oscillation (NAO) (Huang *et al.*, 1998; Li *et al.*, 2013) and the Pacific decadal oscillation (PDO) (Trenberth and Hurrell, 1994). The effects of these phenomena on rainfall (Neupane and Cook, 2013; Zhang and Cook, 2014) and continental temperatures (Wallace *et al.*, 2012; Smoliak *et al.*, 2015) have been thoroughly investigated in recent decades. In particular, a dynamical adjustment method was proposed by Wallace *et al.* (2012), and their results showed that the changes in atmospheric circulation explained approximately 41% of the warming that occurred over land areas poleward of 40°N in the boreal cold season during the significant warming period of 1965–2000.

The thermodynamic temperature is equal to the raw temperature minus the dynamic temperature and is closely related to thermodynamic factors, such as greenhouse gases (GHGs), land use, land cover change (LUCC), and anthropogenic aerosol emissions, many of which are local factors. Many studies have focused on the effects of a single thermodynamic factor. Urban expansion has been

*Correspondence to: X. Guan, Key Laboratory for Semi-arid Climate Change of the Ministry of Education, College of Atmospheric Sciences, Lanzhou University, 222# Tianshui South Road, Lanzhou 730000, China. E-mail: guanxd@lzu.edu.cn

found to lead to marked temperature increases (Qian *et al.*, 2006). Model simulations have revealed that LUCC has potential impacts on local climate variability and climate extremes (Zhang *et al.*, 2009). Moreover, the burning of fossil fuel (Barnett and O'Neill, 2009; Dougill *et al.*, 2010) and agricultural fires produce black carbon particles that affect the warming in winter by significantly reducing the albedo of snow and enhancing the absorption of solar radiation (Lau *et al.*, 2010; Huang *et al.*, 2011; Qian *et al.*, 2011). Large black carbon and organic matter emissions from anthropogenic activities and strong snow feedback have been detected in Asia (Flanner *et al.*, 2009).

Although ESAW has been discussed for several years, little work has been conducted to quantify the effects of various factors on the ESAW processes. In this study, we applied a dynamical adjustment method (Wallace *et al.*, 2012; Smoliak *et al.*, 2015) to the temperature to divide it into dynamic and thermodynamic components. The different behaviours of the dynamic and thermodynamic temperatures may reveal the underlying ESAW mechanism, especially in the three typical semi-arid regions of the mid-to-high latitudes in Asia, Europe, and North America. Moreover, to better understand and highlight the warming effects associated with thermodynamic forcing, the simulated temperatures of the Coupled Model Intercomparison Project Phase 5 (CMIP5) models are investigated in this study.

This study is organized as follows. The datasets and methods used to calculate the warming trend/contribution and the dynamical adjustment methodology are presented in detail in Section 2. The analysis and results are provided in Section 3. Finally, the discussion and conclusions are given in Section 4.

2. Data and methodology

2.1. Observational data

Monthly global land surface air temperature and precipitation data from 1901 to 2011 at the high spatial resolution of $0.5^\circ \times 0.5^\circ$ were obtained from the Climate Research Unit (version TS3.21) at the University of East Anglia (Mitchell and Jones, 2005). The climatological annual precipitation (1961–1990) was used to classify the climate regions because the long-term mean precipitation is the simplest index for this purpose (Fu and An, 2002; Tang *et al.*, 2002; Huang *et al.*, 2012). The climatic regions were defined as follows: arid regions (annual precipitation of $0\text{--}200\text{ mm year}^{-1}$), semi-arid regions (annual precipitation of $200\text{--}600\text{ mm year}^{-1}$) and wet regions (annual precipitation more than 600 mm year^{-1}). Figure 1 shows the spatial distribution of climatological annual precipitation in the latitudinal zone of $20^\circ\text{--}90^\circ\text{N}$. Semi-arid areas cover considerable parts of western North America and Central Asia in the mid-to-high latitudes of the NH. In East Asia, the semi-arid regions are located in the transitional area between the arid and wet regions. Observational sea level pressure (SLP) data were from

the National Oceanic and Atmospheric Administration (NOAA)/Cooperative Institute for Research in Environmental Sciences 20th Century Reanalysis (20CR), version 2; these data have a spatial resolution of $2^\circ \times 2^\circ$ for the period 1901–2011 (Compo *et al.*, 2011).

2.2. Model data

The 20 climate models used in this study are from the CMIP5 and are listed in Table 1. These climate models were introduced in the Intergovernmental Panel on Climate Change Fifth Assessment Report (IPCC AR5) (Taylor *et al.*, 2012). A historical run from 1901 to 2005 and future medium–low scenario simulations from 2006 to 2011 based on the representative concentration pathway (RCP4.5) are used in this study.

2.3. Methods

The temperature trends and contributions in this study were calculated using the methods described in Huang *et al.* (2012). For each climatic region (classified by annual precipitation), the regional average temperature \bar{T}_k in each year was obtained using latitude-weighted temperature averages, as shown in Equation (1), prior to calculating the least squares linear trend:

$$\bar{T}_k = \frac{\sum_{i=1}^{N_k} w_{ki} \times T_{ki}}{\sum_{i=1}^{N_k} w_{ki}} \quad (1)$$

where N_k is the number of grids in region k , T_{ki} is the temperature of grid i in region k , and $w_{ki} = \cos(\theta_i \times \pi/180)$, with θ_i representing the latitude of grid i . By applying the least squares method to the averaged \bar{T}_k series, the temperature trend in each climatic region was obtained. The contribution rate of warming in each climatic region k to the whole region was calculated based on the area-weighted temperature trend fraction using Equation (2):

$$\text{CR}_k = \frac{a_k \sum_{i=1}^{N_k} w_{ki}}{A_g \sum_{i=1}^{N_g} w_i} \quad (2)$$

where a_k is the temperature trend for region k , A_g is the trend over the whole region, N_k is the number of grids in region k , and N_g is the total number of all grids in the whole region.

The dynamical adjustment methodology used in this study was explicitly introduced by Wallace *et al.* (2012) and Smoliak *et al.* (2015) and is based on the partial least squares (PLS) regression of the surface air temperature against the SLP. The PLS regression predicts a dependent variable (predictand) based on a set of independent variables (predictors) and has been applied in various types of climate research, including paleoclimate reconstruction

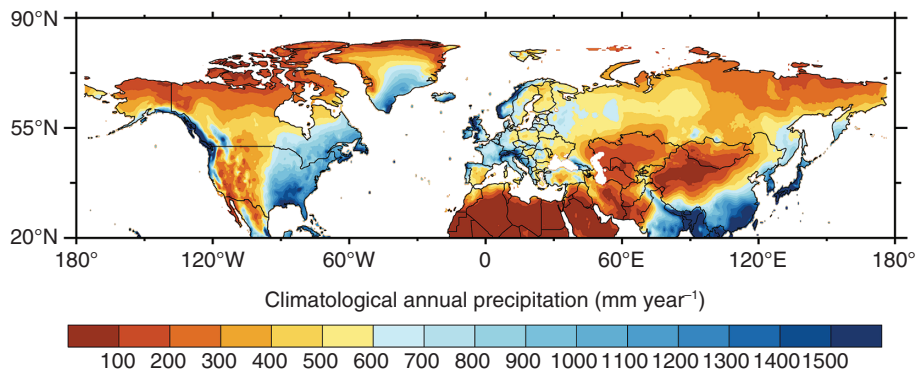


Figure 1. Distribution of climatological (1961–1990) annual mean precipitation.

(Kalela-Brundin, 1999), diagnosing year-to-year variations in snowpack and hurricanes (Smoliak *et al.*, 2010), examining the accelerated warming over the mid-to-high latitudes of the NH (Wallace *et al.*, 2012), and investigating the recent warming hiatus which is effective in revealing the key role played by the dynamic cooling effect in this hiatus (Guan *et al.*, 2015). In this study, the PLS regression is applied in a pointwise manner, i.e. a grid point temperature time series is the predictand (referred to as \mathbf{Y}) and the SLP predictor (referred to as \mathbf{X}) of each temperature grid box is the SLP field within a 60° longitudinal sector centred on the temperature grid box, extending poleward from 20°N. The selected SLP domain follows the result of the SLP domain sensitivity test in Smoliak *et al.* (2015), which was demonstrated to contain most of the important information of the referenced grid box temperature. The temperature time series of each grid \mathbf{Y} and its SLP predictor \mathbf{X} are standardized first. Then, \mathbf{Y} is high-pass filtered before we carry out the following steps: (1) We calculate the correlation coefficient between \mathbf{Y} and \mathbf{X} to form a one-point cross-correlation matrix \mathbf{C} . (2) The monthly, standardized \mathbf{X} is projected onto the cross-correlation matrix \mathbf{C} :

$$\mathbf{S} = \mathbf{X}\mathbf{C} \quad (3)$$

and then weighted \mathbf{S} by the cosine of latitude to obtain a time-varying index of the pattern (i.e. the first PLS predictor $\mathbf{Z1}$). Using standardized predictor data prevents predictors with large variances and low correlations from unduly influencing the linear combination, and the high-pass filter of temperature prevents fitting trends. (3) The PLS predictor $\mathbf{Z1}$ is regressed out of both \mathbf{X} and the ‘unfiltered’ \mathbf{Y} to obtain a set of residual variables ($\mathbf{Y1}$ and $\mathbf{X1}$), which are then used to determine the next PLS predictor:

$$\mathbf{Y}' = \mathbf{K}\mathbf{Z1} \quad (4)$$

$$\mathbf{Y1} = \mathbf{Y} - \mathbf{Y}' \quad (5)$$

$$\mathbf{X}' = \mathbf{K}\mathbf{Z1} \quad (6)$$

$$\mathbf{X1} = \mathbf{X} - \mathbf{X}' \quad (7)$$

Table 1. List of the CMIP5 models examined in this study. The historical run for the period 1901–2005 and the future scenario RCP4.5 from 2006 to 2011 were used.

Model name	Modelling centre
BCC-CSM1.1	Beijing Climate Center, China
CanESM2	Canadian Centre for Climate, Canada
CCSM4	National Center for Atmospheric Research, USA
CNRM-CM5	Centre National de Recherches Meteorologiques, France
CSIRO-Mk3.6.0	Commonwealth Scientific and Industrial Research, Australia
GFDL-CM3	Geophysical Fluid Dynamics Laboratory, USA
GFDL-ESM2G	Geophysical Fluid Dynamics Laboratory, USA
GFDL-ESM2M	Geophysical Fluid Dynamics Laboratory, USA
GISS-E2-R	NASA Goddard Institute for Space Studies, USA
HadGEM2-CC	Met Office Hadley Centre, UK
HadGEM2-ES	Met Office Hadley Centre, UK
INM-CM4	Institute for Numerical Mathematics, Russia
IPSL-CM5A-LR	Institute Pierre-Simon Laplace, France
IPSL-CM5A-MR	Institute Pierre-Simon Laplace, France
MIROC-ESM	Japan Agency for Marine-Earth Science and Technology, Japan
MIROC-ESM-CHEM	Japan Agency for Marine-Earth Science and Technology, Japan
MIROC5	Atmosphere and Ocean Research Institute, Japan
MPI-ESM-LR	Max Planck Institute for Meteorology, Germany
MRI-CGCM3	Meteorological Research Institute, Japan
NorESM1-M	Norwegian Climate Centre, Norway

(4) Use the residual variables $\mathbf{Y1}$ and $\mathbf{X1}$ to repeat steps (1)–(3) to obtain the residual PLS predictors and the high-pass filter is applied to each residual temperature time series $\mathbf{Y1}$ before calculating the cross-correlation matrix. To prevent over-fitting, only the three leading PLS predictors (determined via cross-validation) are retained.

Following the processes stated above, the dynamically induced component associated with changes in atmospheric circulation is identified and is referred to here as ‘dynamic temperature’. The dynamically adjusted component, i.e. the residual after removing the dynamically induced component, is associated with thermodynamic processes and is called ‘thermodynamic temperature’. The adjustment removes most of the variability introduced by variations in the atmospheric circulation such as the annular modes and can be used for climate diagnostic studies of both short-term climate fluctuations and long-term trend. It is worth noting that the SLP considered in the process is over 20°–90°N, variations in the tropical oceans and Southern Hemisphere circulations are not included.

3. Results analysis

Figure 2 presents the temporal variations in temperature anomalies in the raw, dynamic, and thermodynamic temperatures over land poleward of 20°N during boreal cold seasons (November to March) (Figure 2(a)) and boreal warm seasons (May to September) (Figure 2(b)). The raw temperature warming trend in the cold seasons during 1902–2011 is visually apparent (black line). The thermodynamic temperature in the cold seasons exhibits a curve similar to that of the raw temperature but its inter-annual variation is substantially reduced. The dynamic temperature change exhibits a strong year-to-year variability that accounts for much of the inter-annual fluctuation in the raw temperature in the cold seasons. In summer, however, the raw temperature shows smaller warming trend as well as smaller inter-annual variability than that in winter. Due to the weaker dynamical influence of Northern Hemispheric circulation variations in the warm season, the dynamically induced variability is much smaller in the summer (Figure 2(b)) than in the cold seasons. As a result, thermodynamic temperature in summer exhibits the similar time evolution as raw temperature. The dynamic temperature in the cold seasons appears to primarily account for the inter-annual and decadal variability of the raw temperature, whereas the thermodynamic temperature primarily contributes to the long-term warming trend.

Figure 3 displays the spatial distribution of the land surface air temperature trends in the raw, thermodynamic and dynamic temperatures during the cold seasons of 1902–2011. The raw temperature trend was positive in most NH areas poleward of 20°N, except in several small domains (Figure 3(a)). However, this trend was markedly unevenly distributed. The temperature increase was particularly pronounced in the mid-to-high latitudes over Eurasia and North America, where the warming rate exceeded 0.024 °C year⁻¹. The thermodynamic temperature in Figure 3(b) shows a similar warming distribution, with stronger warming than that in the raw temperature over the north of Eurasia and the south of North America. The distribution of dynamic temperature change shown in Figure 3(c) is opposite to that of the thermodynamic temperature: a cooling effect appears poleward of 55°N

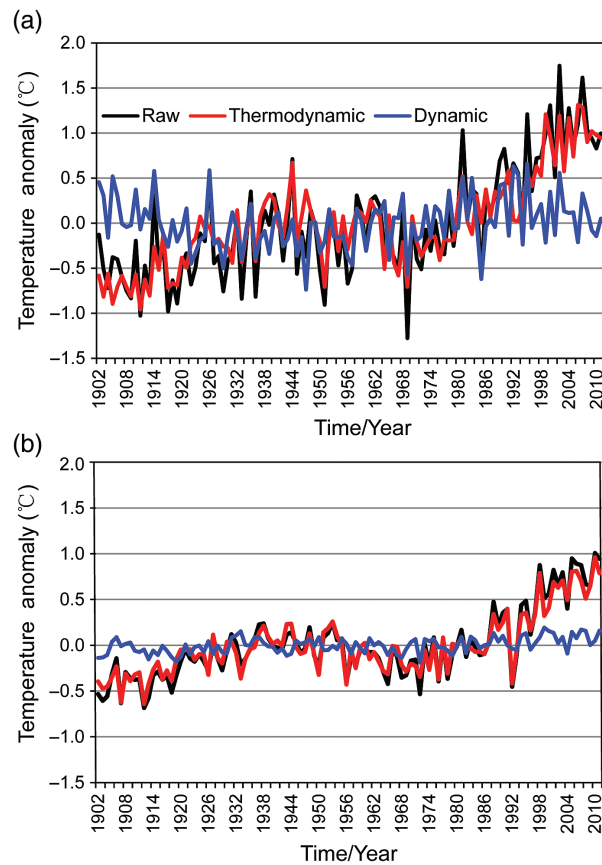


Figure 2. Mean time series of surface air temperature anomalies from 1902 to 2011 in the NH poleward of 20°N during the cold season (November to March) (a) and the warm season (May to September) (b) for the raw (black), dynamic (blue), and thermodynamic (red) temperatures.

over Eurasia, most areas of the US, and Eastern Africa, whereas a warming effect is evident in most of Canada and central and southern Eurasia. The different behaviours of the dynamic and thermodynamic temperatures indicate that the large-scale increase in the thermodynamic temperature plays a major role in the warming process. To study the obvious regional variation in the raw and thermodynamic temperature trends, we selected three semi-arid regions to explore regional warming: Asia, North America, and Europe.

Detailed warming rates of the area-averaged raw, dynamic, and thermodynamic temperatures are listed in Table 2. This table demonstrates that the thermodynamic temperature exhibited larger warming amplitude than the dynamic temperature during 1902–2011. In the regions poleward of 20°N, the area-averaged raw, thermodynamic and dynamic temperatures increased by 1.49, 1.36, and 0.14 °C/109 years, respectively, and the warming amplitude of the thermodynamic temperature was approximately ten times larger than that of the dynamic temperature. The strongest warming was observed in Asia for both the raw (1.85 °C/109 years) and thermodynamic temperatures (1.60 °C/109 years). The second strongest warming area was located in North America, where the raw and thermodynamic temperatures increased by 1.41

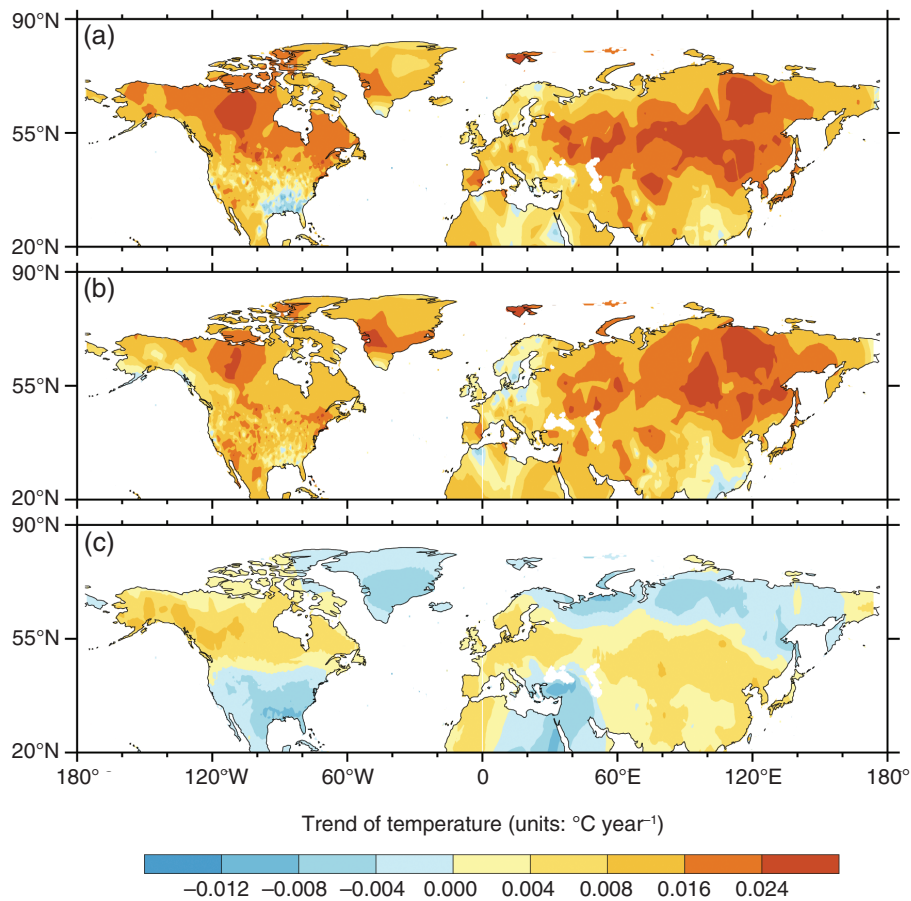


Figure 3. Spatial distribution of the linear surface air temperature trends during the cold season in 1902–2011 for the raw (a), thermodynamic (b), and dynamic temperatures (c).

Table 2. Cold season mean warming amplitudes during 1902–2011 for the raw, thermodynamic, and dynamic temperatures over regions poleward of 20°N in the NH, Asia, Europe, and North America (unit: °C/109 years).

	20°–90°N	Asia	Europe	North America
Raw	1.49	1.85	1.33	1.41
Thermodynamic	1.36	1.60	1.19	1.32
Dynamic	0.14	0.26	0.14	0.09

and 1.32 °C/109 years, respectively. The raw and thermodynamic temperatures in Europe increased by 1.33 and 1.19 °C/109 years, respectively.

Because semi-arid regions within 20°–60°N are the most sensitive to warming (Huang *et al.*, 2012), we calculated the variability of the dynamic and thermodynamic temperatures as a function of the annual precipitation over 20°N–60°N, as shown in Figure 4. The obviously different distributions of the thermodynamic and dynamic temperature trends can be observed in Figure 4(a). Almost all of the dynamic temperature trend points are located in the area with less than 0.01 °C year⁻¹ of warming, whereas most of the thermodynamic trend points are located at warming values greater than 0.01 °C year⁻¹. Additionally, the dynamic temperature trend dots are distributed evenly

in the range of –0.01 to +0.01 °C year⁻¹. In contrast, the amplitudes of the thermodynamic trends are not uniform, and marked trends exceeding 0.02 °C year⁻¹ are concentrated in semi-arid regions, with the largest warming trend reaching 0.05 °C year⁻¹. The regionally averaged thermodynamic and dynamic temperature trends curves show different dependences on the climatological precipitation (Figure 4(b)). The thermodynamic temperature trend increases as the precipitation increases in arid regions and peaks at approximately 300–400 mm year⁻¹ in semi-arid regions before decreasing monotonically as the precipitation continues to increase. However, the dynamic temperature has a relatively flat curve over all precipitation ranges. The higher warming rate of the thermodynamic temperature over semi-arid regions suggests that thermodynamic warming is more sensitive in semi-arid regions and may have induced ESWA in the mid-latitudes of the NH.

The raw, thermodynamic, and dynamic temperature changes as a function of precipitation in Asia, Europe, and North America are compared in Figure 5. These three selected areas exhibit different warming trend curves as a function of precipitation. For the raw temperature trend dependence on annual precipitation (Figure 5(a)), Asia exhibits the strongest semi-arid warming and its warming peaks in the region with annual precipitation of 300–400 mm year⁻¹ and then decreases with the increase

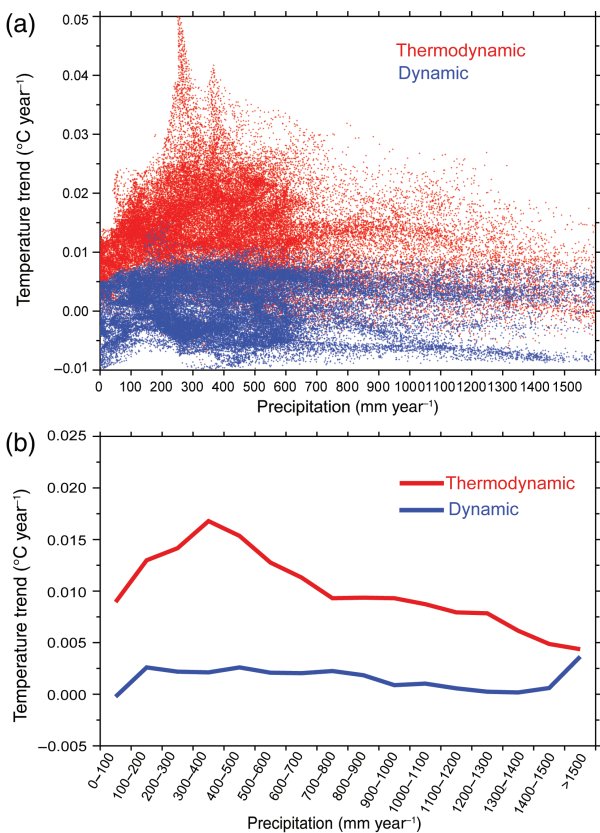


Figure 4. (a) The surface air temperature trend during the cold season in 1902–2011 as a function of the climatological annual precipitation for the thermodynamic (red dots) and dynamic (blue dots) temperatures over the mid-latitudes of the NH (20° – 60° N). (b) The regionally averaged temperature trend in (a).

of annual precipitation. Europe shows smaller warming trend in the semi-arid regions than Asia. In North America, the warming trend dependence on annual precipitation is not as sensitive as that in Asia and Europe. The relationship between thermodynamic temperatures trend and annual precipitation of Asia and Europe (Figure 5(b)) is similar to that in the 20° – 60° N (Figure 4(b), red line), but the warming difference between semi-arid and wet regions is more obvious in Asia than in Europe. In North America, the thermodynamic temperature trend exhibits a relatively weak relationship with annual precipitation, and semi-arid regions with annual precipitation of 400 – 600 mm year⁻¹ do not show obvious thermodynamic warming difference with the wet regions where the annual precipitation are 600 – 1100 mm year⁻¹. In terms of the dynamic temperature variability, a relatively flat change is evident over the regions in Asia and Europe, whereas a much smaller peak than that in the thermodynamic warming appears in the semi-arid regions in North America, suggesting the dominant role of the thermodynamic warming in the semi-arid regions. The different thermodynamic warming behaviours in Asia, Europe, and North America indicate that the variability in the thermodynamic temperature exhibits obvious regional differences. In the three selected regions, Asia exhibits stronger thermodynamic warming

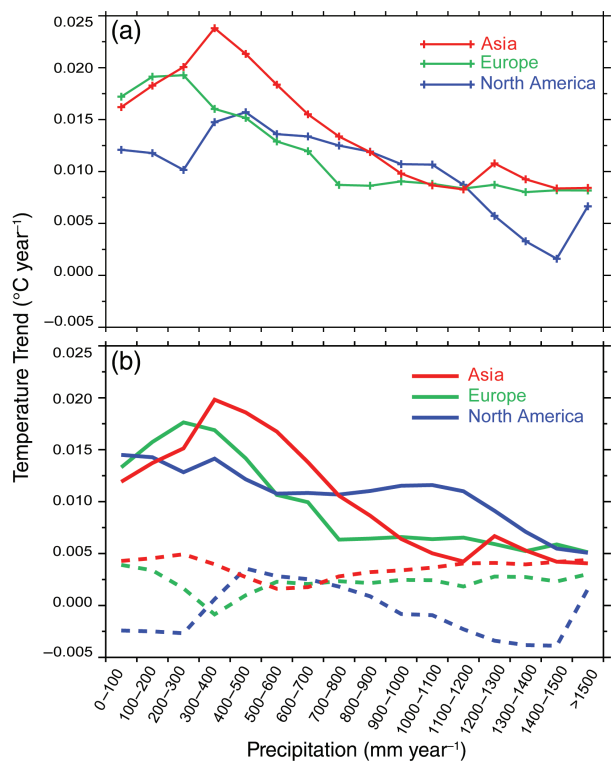


Figure 5. The regionally averaged temperature trend during the cold season in 1902–2011 as a function of the climatological annual precipitation for (a) raw temperature in Asia (red), Europe (green), and North America (blue) and (b) thermodynamic (solid) and dynamic (dashed) temperatures. Asia: 20° – 60° N, 60° – 180° E; Europe: 36° – 60° N, 17° W– 60° E; and North America: 20° – 60° N, 180° – 17° W.

in its semi-arid regions than Europe and North America, suggesting the significant role of ESAW in Asia.

Because of the important role played by the thermodynamic temperature in ESAW, detailed information on the thermodynamic temperature warming amplitudes in semi-arid and wet regions in the mid-latitudes of the NH, Asia, Europe, and North America is presented in Table 3. This table shows that the thermodynamic temperature warmed by 1.63° C/109 years in semi-arid areas from 20° to 60° N. Notably, this value is 2.3 times larger than that in wet regions. Comparison of the warming trends in semi-arid areas in Asia, Europe, and North America reveals that the strongest thermodynamic warming occurred in Asia, where the temperature increase was as high as 1.95° C/109 years, approximately 3.7 times greater than that in wet regions (0.65° C/109 years in Europe and 0.97° C/109 years in North America). Therefore, Asia experienced the largest semi-arid warming trend, which was approximately 1.4 times higher than those in Europe and North America. This obvious difference highlights the thermodynamic warming trend in Asia, which may be strongly related to local thermodynamic factors (Guan *et al.*, 2016).

Table 3. Cold season mean thermodynamic temperature warming amplitudes during 1902–2011 over the mid-latitudes (20° – 60° N) of the NH, Asia, Europe, and North America (unit: $^{\circ}\text{C}/109$ years) in semi-arid and wet regions.

	20° – 60° N	Asia	Europe	North America
Semi-arid regions	1.63	1.95	1.43	1.39
Wet regions	0.72	0.52	0.65	0.97

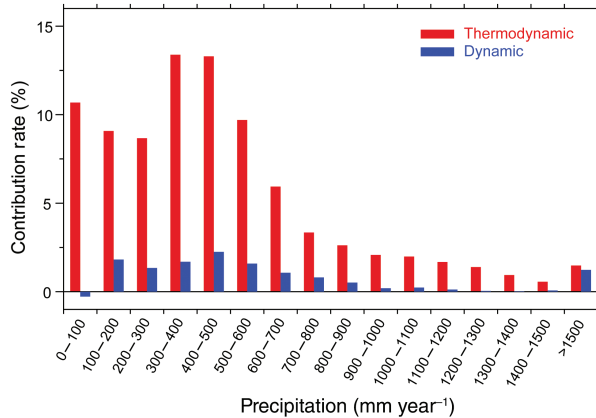


Figure 6. The regional contributions of the dynamic (blue) and thermodynamic (red) land surface air temperature trends to the raw temperature warming over the mid-latitudes of the NH (20° – 60° N) during the cold season in 1902–2011 as a function of the climatological annual precipitation.

To quantify the exact roles of these temperature components in the warming process, we calculated the quantitative warming contributions of the thermodynamic and dynamic temperatures in each climate region to the mean warming of the raw temperature of the 20° – 60° N. Figure 6 illustrates a distinct difference in the contributions of the thermodynamic and dynamic temperatures. The thermodynamic temperature contributed 87.2% of the warming in raw temperature over the 20° – 60° N region, 45.3% of which occurred in semi-arid areas. This contribution was much greater than that of wet regions. In contrast, the dynamic temperature exhibited a considerably weaker contribution than the thermodynamic temperature in all climate regions. The obvious discrepancy between the contributions of the thermodynamic and dynamic temperatures suggests that thermodynamic warming was the primary driver of ESAW in the mid-latitudes of the NH.

Figure 7 presents the contributions of the thermodynamic and dynamic temperatures in each climate region in Asia, Europe, and North America to the warming in the mean raw temperature over the 20° – 60° N region. The thermodynamic temperature contribution far exceeded that of the dynamic temperature in all selected regions, especially in Asia. The thermodynamic temperature in the semi-arid regions in Asia, North America, and Europe contributed 24.7%, 10.9%, and 8.2% to the raw temperature warming over the 20° – 60° N region, respectively. The contributions of the dynamic temperature in these areas were noticeably smaller than those of the thermodynamic

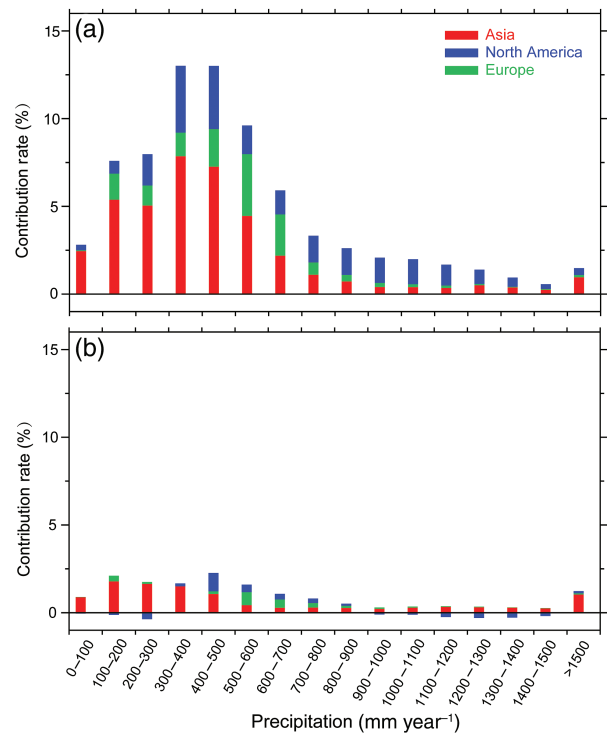


Figure 7. The regional contributions of the thermodynamic (a) and dynamic (b) temperature trends to the raw temperature increase over the mid-latitudes of the NH (20° – 60° N) in the cold season during 1902–2011 as a function of the climatological annual precipitation in Asia (red), Europe (green), and North America (blue).

temperature. This discrepancy in the contributions in Asia, Europe, and North America suggests that local effects play a major role in ESAW, especially in Asia, where frequent anthropogenic activities have contributed greatly to the observed ESAW.

Based on the preceding description and discussion, the thermodynamic temperature plays a dominant role in ESAW. The temporal evolution of the CMIP5 ensemble mean and the observed temperature over 20° – 60° N are compared in Figure 8(a). The change in the ensemble mean temperature time series of CMIP5 could capture the slow temperature increase in the first half century and the rapid warming since 1970s in the observation, indicating that the area-averaged temperature warming was well simulated by the model. However, the spatial distribution of the CMIP5 ensemble mean temperature trend (Figure 8(b)) was relatively homogeneous compared with the observation (Figure 3(a)). The CMIP5 ensemble mean temperature trend is primarily characterized by an increasing warming rate from low to high latitudes, and it exaggerated the warming along the Arctic coast. The CMIP5 ensemble mean simulations did not capture the marked regional non-uniform warming of the observed temperature.

The temperature trends in the simulated, observed raw and thermodynamic temperatures as a function of annual precipitation (Figure 9) show that the ESAW of the observed temperature, which is majorly induced by thermodynamic temperature increase, does not appear in

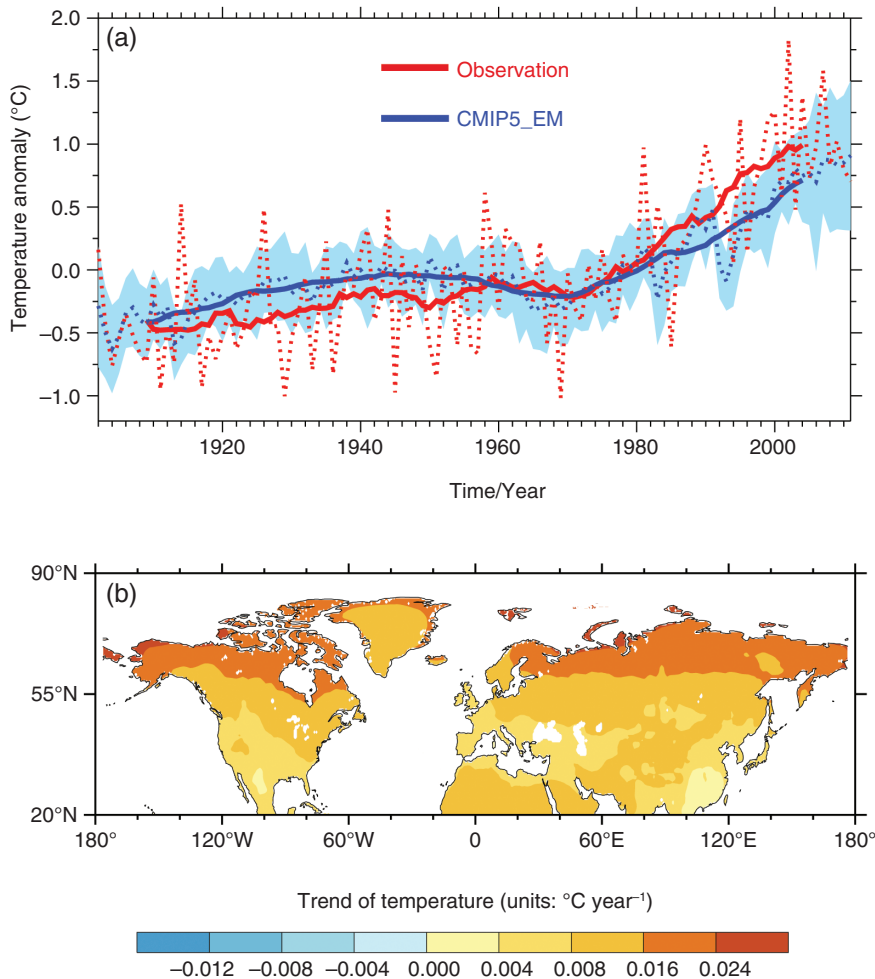


Figure 8. (a) Time series of mean temperature anomalies in the cold season over the mid-latitudes (20° – 60°N) of the NH during 1902–2011 for the observation (red dashed) and the ensemble mean of 20 CMIP5 models (blue dashed). Solid lines indicate the 15-year running means of the dashed lines and blue shading denotes the standard deviation of the temperature simulated by the CMIP5 models. The model data are masked so that they have the same coverage as the observations. (b) Spatial distribution of the temperature trend in the cold season of the ensemble mean of 20 CMIP5 models during 1902–2011.

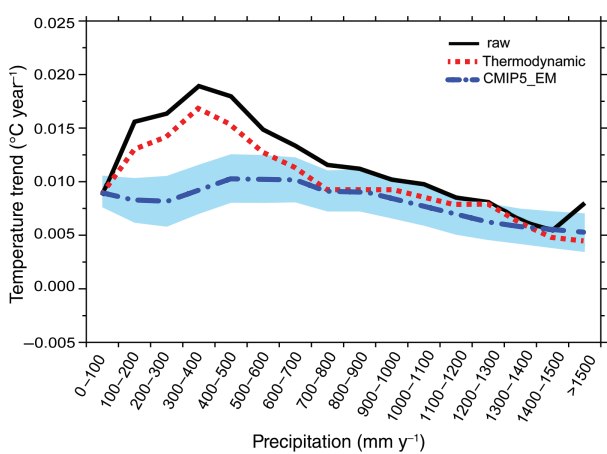


Figure 9. Regionally averaged temperature trends (1902–2011) in the cold season as a function of the climatological annual precipitation over the mid-latitudes (20° – 60°N) of the NH for the raw (black), thermodynamic temperature (red) and the ensemble mean of 20 CMIP5 models. Shading denotes the 95% confidence interval for the different models. The model data are masked so that they have the same coverage as the observations.

the CMIP5 ensemble mean. Indeed, the observed warming amplitude measured in semi-arid areas is approximately 1.8 times greater than that of the CMIP5 simulations. This notable warming bias in semi-arid areas between the observed and the CMIP5-simulated temperatures indicates that some of the local thermodynamic forcing may not thoroughly presented in some CMIP5 models. Based on the CMIP5 distribution of climatological precipitation shown in Figure 10, differences existed between the simulations and observations. Compared with the observations (Figure 1), the CMIP5 values of annual precipitation in semi-arid areas were larger in Asia and North America, especially in the western areas of North America. The trends of simulated temperature as a function of annual precipitation in Asia, Europe, and North America (Figure 11) exhibited relatively flat curves in all regions. The observed temperature warming peaks in semi-arid regions also did not appear in the simulated temperatures in all three selected regions, as well as the obvious discrepancy of warming actions among the three regions.

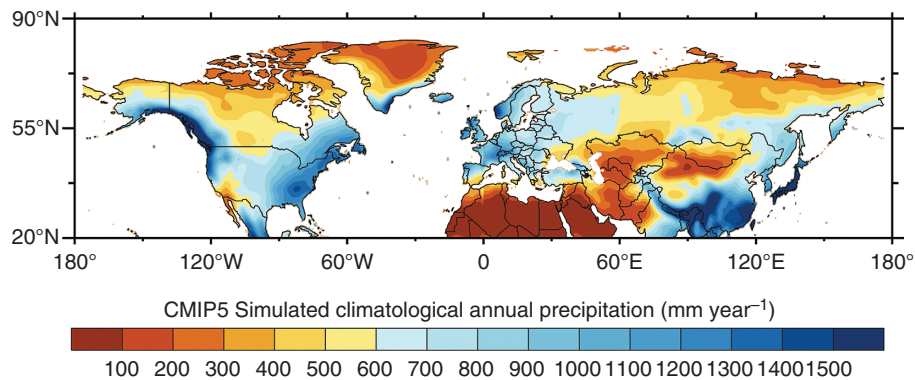


Figure 10. Distribution of the CMIP5 ensemble climatological (1961–1990) mean annual precipitation.

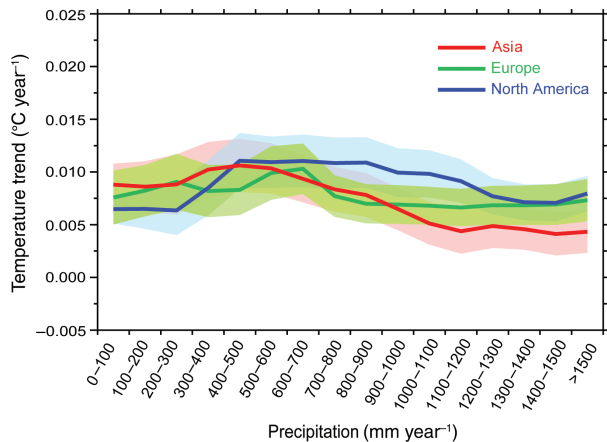


Figure 11. Regionally averaged trends of the CMIP5 ensemble mean temperature in the cold season during 1902–2011 as a function of the climatological annual precipitation over the mid-latitudes (20° – 60° N) in Asia (red), Europe (green), and North American (blue). Shading denotes the 95% confidence intervals for the different models. The model data are masked so that they have the same coverage as the observations.

4. Discussion and conclusions

This study investigated the joint impacts of dynamic and thermodynamic temperature changes on the raw temperature variations in cold seasons of the NH. Over the long term, the dynamic temperature accounted for a substantial portion of the inter-annual and decadal variability in the raw temperature. Conversely, the thermodynamic temperature dominated the significant cold season warming in the NH from 1902 to 2011. The thermodynamic temperature exhibited uneven warming in the different climate regions, with particularly enhanced warming in semi-arid areas. In contrast, the dynamic temperature exhibited a nearly consistent trend over all climate regions. This discrepancy between the thermodynamic and dynamic warming trends reveals the dominant role played by thermodynamic temperature in ESAW, as confirmed by comparing the warming contributions of the dynamic and thermodynamic temperatures. The behaviour of the thermodynamic temperatures in the three selected areas of Asia, Europe, and North America was analysed. The results showed that Asia experienced the greatest temperature increase, with

a higher thermodynamic temperature increase occurring in semi-arid areas than in other regions. However, the obvious ESAW, in which substantial local thermodynamic forcing played a significant role, was not well simulated by the CMIP5 ensemble mean temperature.

Investigation of the CMIP5 simulated temperature changes over Asia, North America, and Europe also indicates that the regional differences of semi-arid warming were not captured in the model simulations. The dominant role of the thermodynamic temperature warming in semi-arid areas indicates that dry lands may suffer from intense human activities that can induce strong local thermodynamic forcing due to the fragile ecosystems in dry lands, which are sensitive to strong interactions between human activities and climate changes (Charney 1975; Huang *et al.*, 2008, 2010; Rotenberg and Yakir, 2010). The semi-arid regions have expanded in the past half century (Feng and Fu, 2013; Li *et al.*, 2015) and Huang *et al.* (2016) projected that the dry lands will continue to expand in the future. Increased aridity, enhanced warming and unreasonable land use under drought conditions in semi-arid regions will cause land degradation and desertification. The feedbacks of desertification, drought and fragile ecosystems in semi-arid regions may, in turn, significantly affect the regional temperature increase. Enhanced warming in semi-arid regions and the warming discrepancies between different semi-arid areas may also be attributable to other thermodynamic processes. Further studies are needed to better understand this issue.

Acknowledgements

This work was supported by the National Science Foundation of China (41575006, 41521004 and 91637312) and the China University Research Talents Recruitment Program (111 project, No. B13045). All authors like to thank Dr. Pu Lin for providing the original code of the dynamical adjustment methodology and thank Dr. Clara Deser for insightful suggestions. All authors would also like to acknowledge the modelling groups, the Program for Climate Model Diagnosis and Intercomparison (PCMDI) and the World Climate Research Programme's (WCRP's)

Working Group on Coupled Modeling for their roles in making CMIP5 model simulations available.

References

- Barnett J, O'Neill S. 2009. Maladaptation. *Glob. Environ. Change* **20**: 211–213.
- Charney J. 1975. Dynamics of deserts and drought in the Sahel. *Q. J. Roy. Meteorol. Soc.* **101**: 193–202.
- Chylek P, Klett JD, Lesins G, Dubey MK, Hengartner N. 2014. The Atlantic multidecadal oscillation as a dominate factor of oceanic influence on climate. *Geophys. Res. Lett.* **41**: 1689–1697.
- Compo GP, Whitaker JS, Sardeshmukh PD, Matsui N, Allan RJ, Yin X, Gleason BE, Vose RS, Rutledge G, Bessemoulin P, Brönnimann S, Brunet M, Crouthamel RI, Grant AN, Groisman PY, Jones PD, Kruk MC, Kruger AC, Marshall GJ, Maugeri M, Mork HY, Nordli Ø, Ross TF, Trigo RM, Wang XL, Woodruff SD, Worley SJ. 2011. The Twentieth Century Reanalysis Project. *Q. J. Roy. Meteorol. Soc.* **137**: 1–28.
- Dougill AJ, Fraser EDG, Reed MS. 2010. Anticipating vulnerability to climate change in dry land pastoral systems: using dynamic systems models for the Kalahari. *Ecol. Soc.* **15**. ISSN: 1708–3087.
- Feng S, Fu Q. 2013. Expansion of global dry lands under a warming climate. *Atmos. Chem. Phys.* **13**: 10081–10094.
- Flanner MG, Zender CS, Hess PG, Mahowald NM, Painter TH, Ramanathan V, Rasch PJ. 2009. Springtime warming and reduced snow cover from carbonaceous particles. *Atmos. Chem. Phys.* **9**: 2481–2497.
- Fu C, An Z. 2002. Study of aridification in Northern China: a global change issue forcing directly the demand of nation (in Chinese). *Earth Sci. Front.* **9**: 271–275.
- Guan X, Huang J, Guo R, Lin P. 2015. The role of dynamically induced variability in the recent warming trend slowdown over the Northern Hemisphere. *Sci. Rep.* **5**: 12669.
- Guan X, Huang J, Zhang Y, Xie Y, Liu J. 2016. The relationship between anthropogenic dust and population over global semi-arid regions. *Atmos. Chem. Phys.* **16**: 5159–5169. <https://doi.org/10.5194/acp-16-5159-2016>.
- Huang J, Higuchi K, Shabbar A. 1998. The relationship between the north Atlantic oscillation and El Niño-southern oscillation. *Geophys. Res. Lett.* **25**: 2707–2710.
- Huang J, Zhang W, Zuo J, Bi J, Shi J, Wang X, Chang Z, Huang Z, Yang S, Zhang B, Wang G, Feng G, Yuan J, Zhang L, Zuo H. 2008. An overview of the semi-arid climate and environment research observatory over the Loess Plateau. *Adv. Atmos. Sci.* **25**: 906–921.
- Huang J, Minnis P, Yan H, Yi Y, Chen B, Zhang L, Ayers JK. 2010. Dust aerosol effect on semi-arid climate over Northwest China detected from A-Train satellite measurements. *Atmos. Chem. Phys.* **10**: 6863–6872.
- Huang J, Fu Q, Zhang W, Wang X, Zhang R, Ye H, Warren SG. 2011. Dust and black carbon in carbon in seasonal snow across northern China. *Bull. Am. Meteorol. Soc.* **92**: 175–181.
- Huang J, Guan X, Ji F. 2012. Enhanced cold-season warming in semi-arid regions. *Atmos. Chem. Phys.* **12**: 5391–5398.
- Huang J, Yu H, Guan X, Wang G, Guo R. 2016. Accelerated dry land expansion under climate change. *Nat. Clim. Change* **6**: 166–171.
- IPCC. 2013. The physical science basis. In *Contribution of Working Group I to the Fifth Assessment Report of the Intergovernmental Panel on Climate Change*, Stocker TF, Qin D, Plattner G-K, Tignor M, Allen SK, Boschung J, Nauels A, Xia Y, Bex V, Midgley PM (eds). Cambridge University Press: Cambridge and New York, NY1535 pp.
- Ji F, Wu Z, Huang J, Chassagne EP. 2014. Evolution of land surface air temperature trend. *Nat. Clim. Change* **4**: 462–466.
- Kalela-Brundin M. 1999. Climatic information from tree-rings of *Pinus sylvestris* L. and a reconstruction of summer temperatures back to AD 1500 in Femundsmarka, eastern Norway, using partial least squares regression (PLS) analysis. *Holocene* **9**: 59–77.
- Lau WKM, Kim M-K, Kim K-M, Lee W-S. 2010. Enhanced surface warming and accelerated snow melt in the Himalaya and Tibetan Plateau induced by absorbing aerosols. *Environ. Res. Lett.* **5**: 025204.
- Li J, Sun C, Jin F. 2013. NAO implicated as a predictor of Northern Hemisphere mean temperature multidecadal variability. *Geophys. Res. Lett.* **40**: 5497–5502.
- Li Y, Huang J, Ji M, Ran J. 2015. Dry land expansion in northern China from 1948 to 2008. *Adv. Atmos. Sci.* **32**: 870–876.
- Mann ME, Steinman BA, Miller SK. 2014. On forced temperature changes, internal variability, and the AMO. *Geophys. Res. Lett.* **41**: 3211–3219.
- Mitchell TD, Jones PD. 2005. An improved method of constructing a database of monthly climate observations and associated high-resolution grids. *Int. J. Clim.* **25**: 693–712.
- Neupane N, Cook KH. 2013. A nonlinear response of Sahel rainfall to Atlantic warming. *J. Clim. Appl. Meteorol.* **26**: 7080–7096.
- Qian L, Cui H, Chang J. 2006. Impacts of land use and cover change on land surface temperature in the Zhujiang Delta. *Pedosphere* **16**: 681–689.
- Qian Y, Flanner MG, Leung LR, Wang W. 2011. Sensitivity studies on the impacts of Tibetan Plateau snowpack pollution on the Asian hydrological cycle and monsoon climate. *Atmos. Chem. Phys.* **11**: 1929–1948.
- Rotenberg E, Yakir D. 2010. Contribution of semi-arid forests to the climate system. *Science* **327**: 451–454.
- Smoliak BV, Wallace JM, Stoelinga MT, Mitchell TP. 2010. Application of partial least squares regression to the diagnosis of year-to-year variations in Pacific Northwest snowpack and Atlantic hurricanes. *Geophys. Res. Lett.* **37**: L03801.
- Smoliak BV, Wallace JM, Lin P, Fu Q. 2015. Dynamical adjustment of the northern hemisphere surface air temperature field: methodology and application to observations. *J. Clim. Appl. Meteorol.* **28**: 1613–1629.
- Sutton RT, Dong BW, Gregory JM. 2007. Land/sea warming ratio in response to climate change: IPCC AR4 model results and comparison with observations. *Geophys. Res. Lett.* **34**: L02701.
- Tang M, Jiang H, Liu Y, Guo W. 2002. Cause analysis of arid region formation on the world (in Chinese). *J. Desert Res.* **22**: 1–5.
- Taylor KE, Stouffer RJ, Meehl GA. 2012. An overview of CMIP5 and the experiment design. *Bull. Am. Meteorol. Soc.* **93**: 485–498.
- Trenberth KE, Hurrell JW. 1994. Decadal atmosphere–ocean variations in the Pacific. *Clim. Dyn.* **9**: 303–319.
- Wallace JM, Fu Q, Smoliak BV, Lin P, Johanson CM. 2012. Simulated versus observed patterns of warming over the extratropical Northern Hemisphere continents during the cold season. *Proc. Natl. Acad. Sci. USA* **109**: 14337–14342.
- Zhang G, Cook KH. 2014. West African monsoon demise: climatology, interannual variations, and relationship to seasonal rainfall. *J. Geophys. Res. Atmos.* **119**: 10175–10193.
- Zhang H, Li Y, Gao X. 2009. Potential impacts of land-use on climate variability and extremes. *Adv. Atmos. Sci.* **26**: 840–854.